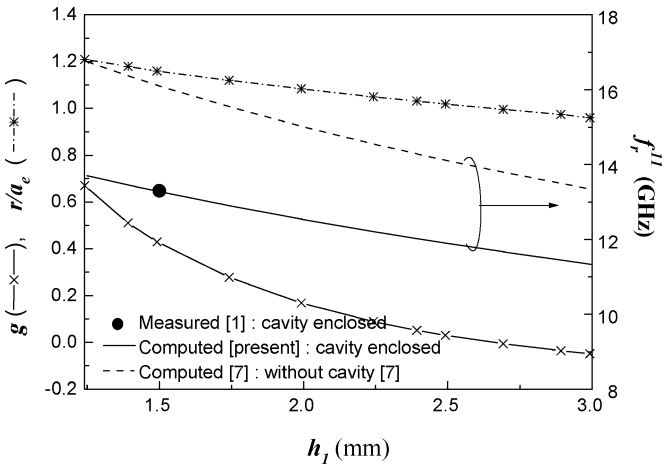

Fig. 3. Resonant frequency of IMCP antenna with and without cavity enclosure and corresponding cavity factors g and r/a_e versus h_1. $r = 6.35$ mm, $h_2 = 1.524$ mm, $\varepsilon_r = 2.3$, $a = 4.0$ mm

for comparison. The increase in h_1 causes decrease in both r/a_e and g values revealing the increasing cavity-effect on the IMCP. The resonant frequency also decreases with the increase in h_1 for both cavity enclosed and open type IMCPs. However, the effect of the cavity enclosure in diminishing the resonant frequency is significant over a considerable range of h_1 values, particularly at the lower values of h_1. Only a single measured value is available [1] to compare with the theoretical curve in Fig. 3 and this value shown by a solid circle corresponds to $g < 0.5$. Excellent agreement between the experiment and the present theory is also revealed.

The present studies show that a cavity enclosure influences the resonance of an IMCP under limited conditions resulting in lower resonant frequency. However, its effect on the radiation characteristics of an IMCP is not significant to that extent as reported in [1]. Uniform radiation patterns with acceptable cross polarization level and 6.65 dBi gain were reported [1] from the measurements of a typical cavity enclosed probe fed IMCP antenna.

IV. Conclusion

The inverted microstrip patches in open or cavity enclosed configuration are attractive for integrating with active devices below it. The change in resonance condition under the influence of a cylindrical cavity enclosing an IMCP has been thoroughly investigated both theoretically and experimentally. If different patches are examined in a same cylindrical enclosure, all are not affected by the cavity and a factor determining that dependence has been examined with the help of the new and previous data. A simple analytical formulation is proposed to predict the resonant frequency of cavity enclosed patches so far those are under the influence of the cavity. The theory is compared with different measurements resulting in very close approximation between them. The studies in this paper thus should guide a designer in choosing proper cavity and IMCP dimensions for a specified frequency within approximately 0.5% accuracy.

Acknowledgment

The authors would like to thank Dr. P. K. Saha and Dr. P. K. Basu of the University of Calcutta for their interest in the work and constant encouragement.

References

[1] J. A. Navarro, L. Fan, and K. Chang, "Active inverted stripline circular patch antennas for spatial power combining," *IEEE Trans Microwave Theory Tech.*, vol. 41, pp. 1856–1863, Oct. 1993.

[2] ——, "Novel FET integrated inverted stripline patch," *Electron. Lett.*, vol. 30, no. 8, pp. 655–657, 1994.

[3] R. A. Flynt, L. Fan, J. A. Navarro, and K. Chang, "Low cost and compact active integrated antenna transceiver for system applications," *IEEE Trans. Microwave Theory Tech.*, vol. 44, pp. 1642–1649, Oct. 1996.

[4] C. M. Montiel, L. Fan, and K. Chang, "A novel active antenna with self-mixing and wideband varactor-tuning capabilities for communication and vehicle identification applications," *IEEE Trans Microwave Theory Tech.*, vol. 44, pp. 2421–2430, Dec. 1996.

[5] J. A. Navarro and K. Chang, "Active microstrip antenna," in *Advances in Microstrip and Printed Antennas*, K. F. Lee and W. Chen, Eds. New York: Wiley, 1997, ch. 8.

[6] J. A. Navarro, J. McSpadden, and K. Chang, "Experimental study of inverted microstrip for integrated antennas applications," in *IEEE Antennas Propagat. Int. Symp. Proc.*, Seattle, WA, 1994, pp. 920–923.

[7] D. Guha and J. Y. Siddiqui, "A new CAD model to calculate the resonant frequency of inverted microstrip circular patch antenna," *Microwave Opt. Technol. Lett.*, vol. 35, no. 6, Dec. 20, 2002.

[8] C. A. Balanis, *Advanced Engineering Electromagnetics*. New York: Wiley, 1989, ch. 9.

[9] I. Wolff and N. Knoppik, "Rectangular and circular microstrip disk capacitors and resonators," *IEEE Trans Microwave Theory Tech*, vol. 22, pp. 857–864, Oct. 1974.

[10] D. Guha, "Resonant frequency of circular microstrip antennas with and without air gaps," *IEEE Trans. Antennas Propaga.*, vol. 49, pp. 55–59, Jan. 2001.

Design and Development of Multiband Coaxial Continuous Transverse Stub (CTS) Antenna Arrays

Robert Isom, Magdy F. Iskander, Zhengqing Yun, and Zhijun Zhang

***Abstract*—Continuous transverse stub (CTS) technology has been adapted to use with coaxial lines to produce effective microwave antenna structures that radiate omnidirectionally, with high efficiency, low reflection, and useful radiation patterns. In this paper, we describe the design, construction, and testing of a new type of antenna arrays, that is, a six-element multiband (4.2 and 19.4 GHz) CTS antenna array. The design of the CTS array was optimized through simulation using finite-difference time-domain and then built and tested using both S-parameters and radiation pattern measurements. Simulation results agreed very well with measured data. These simple and low cost coaxial CTS structures could be adapted for base station applications in wireless communication, for satellite communication systems, and Identification Friend-or-Foe systems for the military.**

***Index Terms*—Antenna array, coaxial continuous transverse stub (CTS), continuous transverse stub (CTS), multiband array.**

I. Introduction

Continuous transverse stub (CTS) technology developed in the early 1990s at Hughes Aircraft Company [1] has attracted research attentions recently [2], [3]. This technology offers advantages over traditional approaches to antenna design at microwave frequencies. Benefits of CTS

Manuscript received May 1, 2003; revised October 21, 2003.

R. Isom is with the Antenna Department, Raytheon Systems, M/S 8019, McKinney, TX 75071 USA.

M. F. Iskander, Z. Yun, and Z. Zhang are with the Hawaii Center for Advanced Communication, College of Engineering, University of Hawaii, Honolulu, HI 96822 USA (e-mail: iskander@spectra.eng.hawaii.edu)

Digital Object Identifier 10.1109/TAP.2004.832336

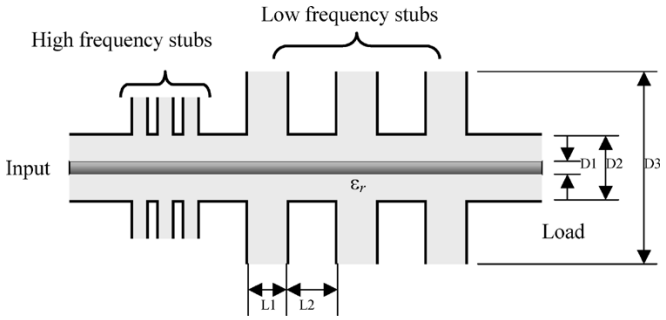

Fig. 1. Schematic of a six-element multiband coaxial CTS antenna array. First set of stubs from input are high-frequency stubs. Second set of stubs from input are low-frequency stubs.

Fig. 2. Photograph of fabricated multiband six-element coaxial CTS antenna array designed to operate at 4.2 and 19.4 GHz: angled view.

structures include compact size, lightweight, low loss, and high directivity. Parallel-plate CTS arrays have achieved average gains of 39.7 dB over a bandwidth of 37–40 GHz [2]. This high gain is achieved along with relative dimensional insensitivity, thus reducing fabrication costs.

CTS technology also offers greater tunable bandwidth than waveguide or patch antennas, higher efficiencies, and polarization isolation of 25–50 dB. It is desired to apply the advantages of the presently available planar CTS technology to a new design that incorporates coaxial geometries. Such a process has been successfully implemented and some of the obtained results for a new coaxial CTS antenna were reported elsewhere [4], [5].

Coaxial CTS structures offer several additional advantages over planar CTS. They provide an omni-directional radiation pattern in the plane of the radiating stubs (perpendicular to the transmission line) as there is no azimuthal dependence in the designed cylindrical stubs. Secondly, coaxial structures are inherently easier to impedance match, thus providing higher efficiency and facilitate system integration with other coaxial structures.

In this paper, a two-band coaxial CTS is designed by simulating different structures using the two-dimensional finite-difference time-domain (2-D-FDTD) code. A prototype antenna is then constructed and tested. The measured S-parameters and radiation patterns agree well with the simulated results.

II. Coaxial CTS Design Procedure

Design procedures for a coaxial CTS array include choosing the following parameters for both of the high- and low-frequency sections (see Fig. 1): 1) width of stub segment: L1; 2) length of transmission line between stubs: L2; 3) dielectric constant of fill material: ε_{r}; 4) diameter of inner conductor: D1; 5) diameter of outer conductor: D2; and 6) diameter of radial stub: D3. To help characterize the antenna performance as we vary some or all of these design parameters, a 2-D axially symmetric cylindrical FDTD code was used to simulate the performance and characterize the many tradeoffs involved in the design of these antennas. For the arrays we designed in this paper, we first designed two separated three-element arrays one at the lower frequency (4.2 GHz) while the other was designed at 19.4 GHz. The two sections were then joined and the entire six-element array was optimized to achieve the desired S-parameters and radiation pattern characteristics. The design of each of the two sections follows a procedure similar to that described in an earlier paper [5], and the discussion in this paper will focus on the design of the six-element multiband array.

III. Design of a Multiband Coaxial CTS Antenna Array

The multiband array is a six-element coaxial CTS array with three elements designed to operate at 4.2 GHz and the other three elements at 19.4 GHz. This array was designed to provide low reflection, high-radiation efficiency, and a broadside radiation pattern at two frequencies, 4.2 GHz (*C*-band) and 19.4 GHz (*K*-band). In designing this array, we used dielectric loading (Teflon and polyethylene) to improve the performance and reduce the overall size of the array.

As mentioned earlier, two sets of stubs were designed: one that was nonradiating (full transmission) at lower frequencies and radiates effectively at higher frequencies (high-frequency stubs), and a second set of stubs that radiate at the lower frequency (low-frequency stubs). The two sets need to be arranged in tandem with the high-frequency stubs near the input. This way, high-frequency signals would radiate from the high-frequency stubs before reaching the low-frequency stubs at the end, and the low-frequency signal, on the other hand, would efficiently pass through the high-frequency stubs connected to the input, and the input low-frequency signal will radiate when reaching the low-frequency stubs at the end of the array.

To accomplish this, it was necessary to know the electrical dimensions that would produce full transmission for the high-frequency stubs at the lower frequency. For this purpose, structures with narrow gaps and long stub diameters were simulated. It was found that narrow gap ($\ll \lambda$) stubs with a stub diameter of approximately $\lambda/3$ (12 mm at 8 GHz) or longer will produce close to full transmission at the lower frequencies. At higher frequencies, however, the same physical dimensions of the stubs were found to radiate efficiently. It is therefore possible to design a coaxial CTS structure that produces efficient radiation at a high frequency and appears almost transparent at lower frequencies.

Using this approach, we simulated a coaxial CTS array with multiband performance. The designed array was dielectrically loaded with Teflon and polyethylene to help improve impedance matching and reduce the size. Further performance enhancements for the multiband array were achieved by controlling design parameters such as the stub gap, stub height, and stub spacing of both the high-and low-frequency stubs. The entire multiband array was further optimized to account for the mutual coupling effects.

Following a manual optimization using inhouse FDTD codes [5], a multiband coaxial CTS antenna array design was achieved that produced low reflection and good radiation characteristics at both the upper and lower frequency bands. The dimensions of the high-frequency stubs were $\mathrm{L1} = 5.2\ \mathrm{mm}$, $\mathrm{L2} = 3.8\ \mathrm{mm}$, $\mathrm{D1} = 1.12\ \mathrm{mm}$, $\mathrm{D2} = 3.6\ \mathrm{mm}$, and $\mathrm{D3} = 44.4\ \mathrm{mm}$. The dimensions of the low-frequency stubs were $\mathrm{L1} = 18.9\ \mathrm{mm}$, $\mathrm{L2} = 29.6\ \mathrm{mm}$, $\mathrm{D1} = 1.12\ \mathrm{mm}$, $\mathrm{D2} = 3.6\ \mathrm{mm}$, and $\mathrm{D3} = 61.2\ \mathrm{mm}$. The spacing between the last high-frequency stub and the first low-frequency stub in the tandem connection of the two arrays was 21.6 mm. The radial waveguide stubs were dielectrically loaded with Teflon rings. The coaxial line of the multiband array was filled with polyethylene. The Teflon (stubs) and polyethylene (coaxial line) were both simulated with $\varepsilon_{\mathrm{r}} = 2.2$ and $\tan\delta \sim 0$ (negligible dielectric losses). Fig. 1 shows a schematic of the designed multiband six-element array, and Fig. 2 shows a photograph of the fabricated and tested array.

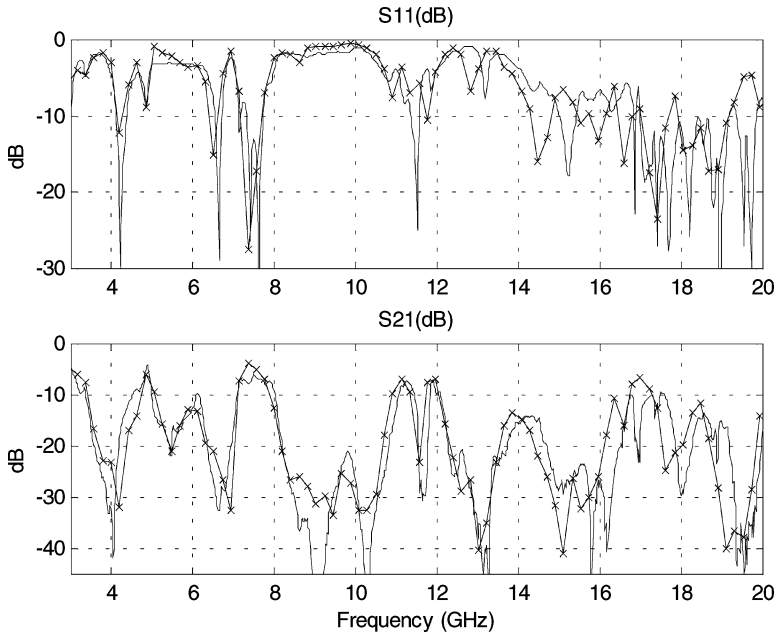

Fig. 3. Comparison of simulated (solid with +) and measured (solid) S-parameter performance for six-element multiband coaxial CTS antenna array. Design frequencies are 4.2 GHz (*C*-band) and 19.4 GHz (*K*-band).

Following fabrication of the six-element multiband coaxial CTS antenna array, the physical dimensions of the structure were measured and found to be in accord with the design parameters. There was a slight air gap between the machined Teflon rings and the polyethylene-filled coaxial transmission line at the base of the stub. A new FDTD model that matched these measured physical dimensions and included the deviations from the initial design was then simulated. Simulations results were then compared with the measured S-parameters and radiation patterns for the fabricated prototype array.

Measurements of the coaxial CTS array were taken using the HP 8510B Network Analyzer. The S-parameters were characterized across 3–20 GHz band. These experimental results are shown along with the simulation S-parameter results obtained using FDTD in Fig. 3. As may be noted, there is a good agreement of resonant frequency performance between measurement and simulations. The multiband array was found to possess $S_{11} = -33$ dB and 98% radiated power ($S_{21} < -20$ dB) in the lower band at 4.2 GHz. The multiband array was found to possess S_{11} over -60 dB and 98% radiated power in the upper band at 19.4 GHz. The 10-dB bandwidth (where $S_{11} < -10$ dB, VSWR < 2) was found to be 6% (~ 250 MHz) in lower band and 12% (~ 2.2 GHz) in the upper band.

The radiation pattern of the six-element multiband coaxial CTS antenna array was also measured at 4.2 GHz (see Fig. 4). The measured radiation pattern produced broadside patterns, useful for many applications. There was a slight rotation in the radiation pattern away from the source ($\theta = 180^\circ$). This deviation from the simulated results was small and did not change the broadside nature of the pattern or produce significant changes in the side lobe levels. The radiation pattern at 19.4 GHz was also measured in anechoic chamber (see Fig. 5) and found to be in agreement with simulation results. Increased side lobe levels in the 19.4 GHz pattern are seen toward endfire (at 180°) due to the effect of the feed cable and connectors. This effect was not significant enough to change the main broadside nature of the pattern or the maximum side lobe level as shown in Fig. 5.

Good agreement between simulated and measured results was seen for both S-parameter and radiation performance. For both simulated and measured results, the multiband coaxial CTS antenna array was seen to produce low reflection ($S_{11} < -20$ dB) and good radiation

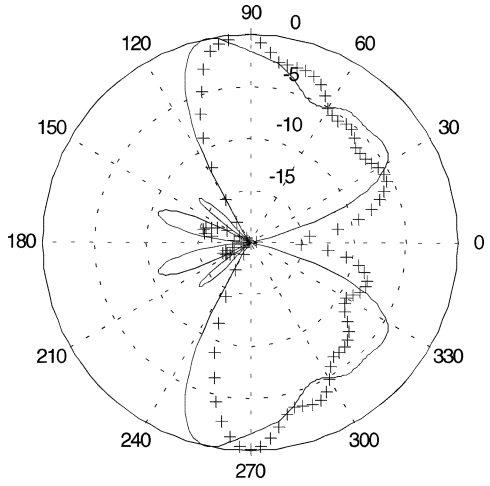

Fig. 4. Comparison of measured (+s) and simulated (solid) radiation pattern at 4.2 GHz for the six-element multiband coaxial CTS antenna array. Feed is from 0°. Displayed on a dB-scale normalized to 0 dB.

characteristics (98% power radiated) at both 4.2 and 19.4 GHz. This validates the multiband design and illustrates the usefulness of the two-dimensional FDTD axially symmetric code as a design tool for coaxial CTS structures.

IV. Tolerance Analysis

Planar CTS technology allows for relatively large tolerances in fabrication without significant alteration in the antenna performance. This dimensional insensitivity is critical to achieving low cost fabrication. It was important to determine if coaxial CTS structures possessed the same relative dimensional insensitivity.

Small changes were made in the simulation models, representing deviations from the design dimensions, and FDTD simulations were run with these changes included both as increases and decreases from the design dimensions. These changes were performed on all physical dimensions at the same time. S-parameter results were compared to original design results. It was found that even by allowing for a large tolerance as 5–10 mils, coaxial CTS structures maintained their antenna

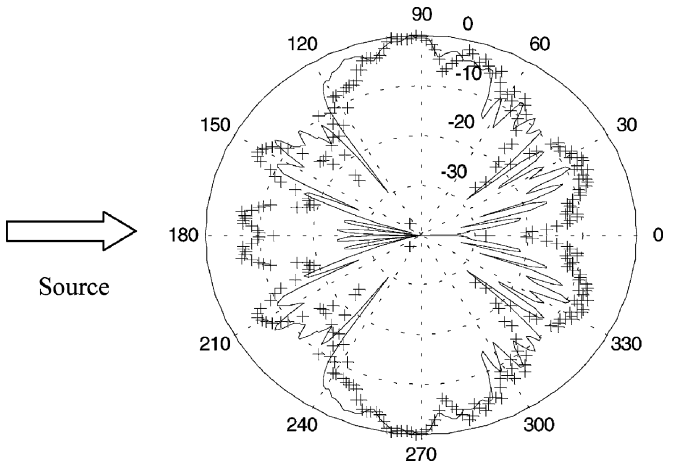

Fig. 5. Comparison of measured (+s) and simulated (solid) radiation pattern at 19.4 GHz for the six-element multiband coaxial CTS antenna array. Feed is from 180°. Displayed on a dB-scale normalized to 0 dB.

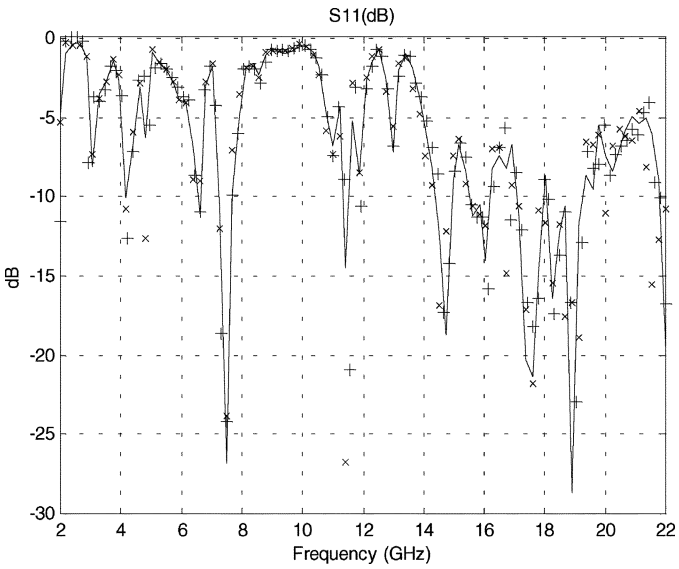

Fig. 6. Plot showing change in S_{11} for small changes in the physical dimensions of the six-element multiband coaxial CTS array. The solid line represents the original simulation. The +s represent a decrease in size from the original dimensions. The Xs represent an increase in size from the original dimensions.

performance and impedance matching characteristics at the design frequencies.

Specifically, FDTD simulation tests were run on three cases for the six-element multiband array. These cases consisted of simulation at the design specifications, simulation at dimensions one cell size (.129 mm or 5 mils) larger than the design specifications, and simulation at dimensions one cell size smaller than the design specifications. The results of the simulations for S_{11} are shown in Fig. 6. These results show that despite some small variation in the S-parameter performance of the array, its overall antenna performance was maintained in the regions around the design frequencies.

We also simulated the effect of small variations in the dielectric constant of the Teflon-filled multiband antenna array on the antenna performance. A simulation was performed using the expected value of Teflon ($\varepsilon_r = 2.1$), while two others were made using somewhat smaller and larger values for Teflon ($\varepsilon_r = 2.0$ and 2.2, respectively). The variations represent a change in the dielectric constant of approximately 5%. The results of these simulations are shown in Fig. 7. As it may be seen, coaxial CTS array is also robust and relatively insensitive to small changes in the dielectric constant of filling material.

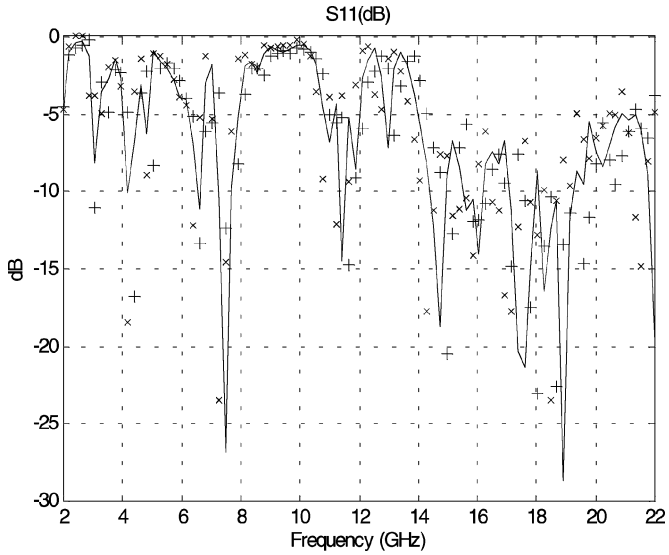

Fig. 7. Plot showing change in S_{11} for small changes in the dielectric constant of the six-element coaxial CTS array. The solid line represents $\varepsilon_r = 2.1$. The +s represent $\varepsilon_r = 2.0$. The Xs represent $\varepsilon_r = 2.2$.

V. Conclusion

Coaxial CTS technology provides low cost, high-efficiency antenna arrays and with excellent radiation and S-parameter characteristics. The radial stubs of coaxial CTS arrays provide an omni-directional pattern in the plane perpendicular to the coaxial line. Coaxial CTS structures also possess the added advantages of ease of impedance matching, ease of feed, and maintains the insensibility to dimensional and dielectric constant tolerances.

In this paper, the design, construction and testing of a multiband antenna array was described. S-parameter performance from 3–20 GHz was measured using the HP8510B Network Analyzer. Good agreement was achieved between simulated S-parameter results obtained using FDTD and measured results, particularly at the desired multiband frequencies of 4.2 and 19.4 GHz. The measured and simulated results confirmed that it was possible to obtain low reflection, high-radiation efficiency, and good radiation pattern at frequencies in two different bands (*C*-band and *K*-band).

Radiation pattern measurements were also taken at 4.2 and 19.4 GHz and the broadside radiation pattern characteristic was verified. Several simulations were also performed to confirm the dimensional tolerance, and hence emphasize the low cost fabrication advantage of the coaxial CTS antenna design.

The excellent radiation performance shown by the coaxial CTS antenna arrays would enable many high-frequency communication applications for both military and commercial use. In particular, such high-efficiency antenna arrays would be useful for close range wireless connectivity (e.g., Bluetooth). Additionally, this technology has potential military application (e.g., Identification Friend-or-Foe (IFF) systems). They are compact in size and lightweight. Potentially, beam-steering capability can be accomplished in the same manner as planar CTS designs, either mechanically or using Ferroelectric materials.

References

[1] W. W. Milroy, "The continuous transverse stub (CTS) array: Basic theory, experiment and application," in *Proc. Antenna Applications Symp.*, Allerton Park, IL, Sept. 25-27, 1991.

[2] ——, "Continuous transverse stub element devices and methods of making same," U.S. Patent 5 266 961, Aug. 29, 1991.
[3] M. F. Iskander, Z. Yun, Z. Zhang, R. Jensen, and S. Redd, "Design of a low-cost 2-D beem-steering antenna using ferroelectric material and the CTS technology," *IEEE Trans. Microwave Theory Tech.*, vol. 49, pp. 1000–1003, May 2001.
[4] Z. Zhang, M. F. Iskander, and Z. Yun, "Coaxial continuous transverse stub element device antenna array and filter," U.S. Patent 6 201 509, Nov. 5, 1999.
[5] M. F. Iskander, Z. Zhang, Z. Yun, and R. Isom, "Coaxial continuous transverse stub (CTS) array," *IEEE Microwave Wireless Component Lett.*, pp. 489–491, Dec. 2001.

Near-Field, Spherical-Scanning Antenna Measurements With Nonideal Probe Locations

Ronald C. Wittmann, Bradley K. Alpert, and Michael H. Francis

***Abstract*—We introduce a near-field, spherical-scanning algorithm for antenna measurements that relaxes the usual condition requiring data points to be on a regular spherical grid. Computational complexity is of the same order as for the standard (ideal-positioning) spherical-scanning technique. The new procedure has been tested extensively.**

***Index Terms*—Near-field measurements, probe-position correction, spherical scanning.**

I. Introduction

As frequency increases and wavelength decreases, it becomes difficult to maintain mechanical tolerances in near-field scanning antenna measurements. Therefore, the paradigm shifts from taking measurements at predefined locations to accurately determining the positions where measurements are actually made. Standard algorithms for transformation from near-field to far-field require that data points lie on a regular grid. Our goal is to relax this condition without increasing computational complexity or sacrificing accuracy. Previously, we have dealt with planar near-field scanning [1]. Here, we turn our attention to spherical near-field scanning [2] . Although the details are different, the basic approach is the same: The technique relies on efficient linear transformation between spherical-mode coefficients and probe response at actual measurement locations. The conjugate-gradient method is applied to determine the coefficients that produce a weighted-least-squares match to the measured probe response. In the following, we sketch the theory and demonstrate the algorithm through numerical simulation.

II. Theory

The electric field of an antenna, operating at frequency $f = \omega/2\pi$, may be expressed as an expansion of spherical waves

$$\mathbf{E}(\mathbf{r}) = \sum_{n=1}^{N} \sum_{m=-n}^{n} \left[b^1_{nm} \mathbf{m}_{nm}(\mathbf{r}) + b^2_{nm} \mathbf{n}_{nm}(\mathbf{r}) \right] \tag{1}$$

where the vector modal (Hansen) functions $\mathbf{m}_{nm}$ and $\mathbf{n}_{nm}$ are described in [3, Ch. 7], for example, and the coefficients b^1_{nm} and b^2_{nm} completely characterize the radiated electromagnetic fields of the test antenna. The time-dependent factor $\exp(-i\omega t)$ has been suppressed. Equation (1) is valid in free space outside the minimum sphere; that is, outside the smallest sphere centered on the coordinate origin that encloses the radiating structure. The summation over n must be truncated for practical reasons. Normally, it suffices to choose $N \sim ka$, where a is the radius of the minimum sphere and $k = 2\pi/\lambda = \omega/c$.

Manuscript received August 19, 2003.

The authors are with the National Institute of Standards and Technology, Boulder, CO 80305 USA (e-mail: wittmann@boulder.nist.gov).

Digital Object Identifier 10.1109/TAP.2004.832316

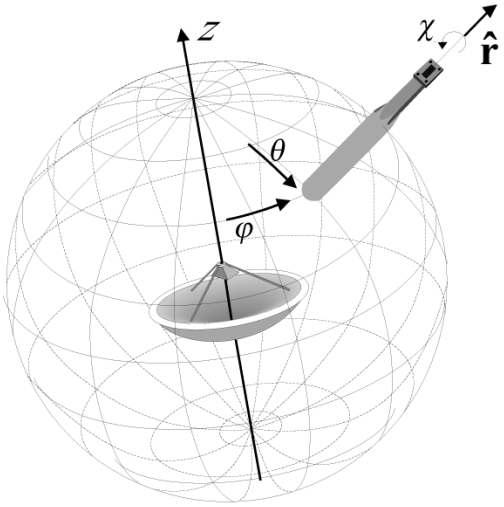

Fig. 1. Spherical scanning geometry.

In spherical scanning, the probe is effectively moved over the surface of a sphere of radius r so that it always "points" in the radial direction $-\hat{\mathbf{r}}$. As shown in Fig. 1, the probe's position and orientation is described by the Euler angles (φ, θ, χ), where θ and φ are the usual spherical-coordinate angles that define the location of the probe. The angle χ measures rotation of the probe about $\hat{\mathbf{r}}$. We assume that the receiving pattern is broad enough that small pointing errors are unimportant. Although possible in principle, correcting for probe wobble would be costly in terms of measurement and processing time.

In order to simplify the collection and processing of measurement data, we follow common practice [4] and restrict our attention to special probes that have a response $w(r, \varphi, \theta, \chi)$ with a simple χ dependence

$$w(r, \varphi, \theta, \chi) = -w(r, \varphi, \theta, -\pi/2) \sin\chi + w(r, \varphi, \theta, 0) \cos\chi. \tag{2}$$

Such probes are not difficult to construct [5, Ch. 1]. They are called $\mu = \pm 1$ probes for reasons that may not be clear in this context. An example is a probe that measures transverse components of the electric field with, say, $E_\varphi = w(r, \varphi, \theta, 0)$ and $E_\theta = w(r, \varphi, \theta, -\pi/2)$. Any practical probe will approach a $\mu = \pm 1$ probe as r is increased.

The Jensen transmission formula [4] expresses the measurement vector $\mathbf{w}(\mathbf{r})$ as an expansion in spherical harmonics

$$\begin{aligned} \mathbf{w}(\mathbf{r}) &\equiv w(r, \varphi, \theta, -\pi/2)\hat{\boldsymbol{\theta}} + w(r, \varphi, \theta, 0)\hat{\boldsymbol{\varphi}} \\ &= \sum_{nm} \left[B^1_{nm}(kr) \mathbf{X}_{nm}(\hat{\mathbf{r}}) + B^2_{nm}(kr) \mathbf{Y}_{nm}(\hat{\mathbf{r}}) \right] \end{aligned} \tag{3}$$

where

$$\begin{pmatrix} B^1_{nm} \\ B^2_{nm} \end{pmatrix} = \mathbf{M}_n \begin{pmatrix} b^1_{nm} \\ b^2_{nm} \end{pmatrix}. \tag{4}$$

In (4), $\mathbf{M}_n$ is a known 2×2 matrix depending on r and the probe receiving function. The vector spherical harmonics $\mathbf{X}_{nm}$ and $\mathbf{Y}_{nm} = i\hat{\mathbf{r}} \times \mathbf{X}_{nm}$ are defined by Jackson [6].

Using (2), (3), and (4), we write

$$\mathbf{W} = \mathbf{A}\mathbf{b}. \tag{5}$$